Chapter 10

Manufacture and Development of Nanostructured Diamond Tools

M. J. Jackson, W. Ahmed and J. S. Morrell

10.1 Introduction

Chemical vapor deposited diamond films have many industrial applications but are assuming increasing importance in the area of microfabrication, most notably in the development of diamond-coated micro-tools. For these applications the control of structure and morphology is of critical importance. The crystallite size, orientation, surface roughness, and the degree of sp^3 character have a profound effect on the machining properties of the films deposited. In this paper experimental results are presented on the effects of nitrogen doping on the surface morphology, crystallite size, and wear of micro-tools. The sp^3 character optimises at 200 ppm of nitrogen and above this value the surface becomes much smoother and crystal sizes decrease considerably.

Fracture induced wear of the diamond grain is the most important mechanism of material removal from a micro-grinding tool during the grinding process. Fracture occurs as a consequence of tensile stresses induced into diamond grains by grinding forces to which they are subjected. The relationship between the wear of diamond coated grinding tools, component grinding forces, and induced stresses in the model diamond grains is described in detail. A significant correlation is found between the maximum value of tensile stress induced in the diamond grain and the appropriate wheel-wear parameter (grinding ratio) machining a selection of engineering steels and cast iron materials. It is concluded that the

magnitude of tensile stresses induced in the diamond grain by grinding forces at the rake face is the best indicator of tool wear during the grinding process. Diamond has a unique combination of excellent physical and chemical properties, which makes it ideal for numerous applications [1-3]. It can be used in biomedical components, cutting tools, optical components, microelectronic circuits and thermal management systems. A number of methods have been investigated in order to deposit diamond in thin form to various substrates, the most common being silicon and tungsten carbide cemented with a small amount of cobalt metal [4-6]. Arguably, the most successful method of depositing polycrystalline films of diamond is chemical vapor deposition (CVD). In this paper we investigate a variant of the basic CVD process known as hot filament CVD for the deposition of diamond. It is generally agreed that the properties of the films, such as morphology, quality, and adhesion that determine the suitability for use in a particular application [7]. In the case of micro-tools, extremely small particles of diamond are required that are blocky in form so that cutting of metals and other materials can be performed with relative ease. Both the diamond nucleation stage and the CVD process conditions critically affect the structure and morphology of diamonds. Abrasion of the substrate material with diamond powder prior to deposition is commonly used to enhance the diamond nucleation density [8-10]. However, such abrasion methods damage the surface in a poorly defined manner. Thus, more controlled methods of nucleation such as biasing prior to CVD are becoming increasingly common [11,12] and can even enable heteroepitaxial growth of diamond films [13,14]. The gas-phase environment during deposition also affects the quality and morphology of the resulting diamond films. The addition of nitrogen [15,16], boron [17] and phosphorus [18] containing gases to the standard methane/hydrogen gas mixtures can change crystal size and its faceting. The effect of changing the stoichiometric balance of the mixture of gases has a significant effect on the development of wear in micro-tools. Wear mechanisms in micro-tools appear to be similar to that of single-point cutting tools, the only difference being the size and nature of swarf generated. Micro-tools contain very small sharp abrasive grains with blunted cutting edges (known as wear flats), and

diamond grains with sharp cutting edges that are released from the grinding tool before they had a chance to remove material from the workpiece. The general form of the wear curve is similar to that of a single-point cutting tool. The wear behavior observed is similar to that found in other wear processes; high initial wear followed by steady-state wear. A third accelerating wear regime usually indicates the occurrence of catastrophic wear of the tool. This type of wear is usually accompanied by thermal damage to the surface of the machined workpiece, which reduces fatigue strength and the life of the component. The performance index used to characterise wear resistance is the grinding ratio, or G-ratio, and is expressed as the ratio of the change in volume of the workpiece ground, Δv_w, to the change in the volume of the surface of the tool removed, Δv_s, and is shown in Eq. (10.1),

$$G = \Delta v_w / \Delta v_s \tag{10.1}$$

Grinding ratios cover a wide range of values ranging from less than one for high speed steels [19] to over 60,000 when internally grinding bearing races using cubic boron nitride abrasive wheels [20]. Attempts have been made to address the problems related to the wear of abrasive grains in terms of the theory of brittle fracture [21]. The conclusions of various researchers lead us to believe that the variety of different and interacting wear mechanisms involved, namely, plastic flow of abrasive, crumbling of the abrasive, chemical wear, etc., makes grinding tool wear too complicated to be explained using a single theoretical model [22]. The following analysis of diamond grains represented by single-point loaded wedges assumes that diamond grain fracture is the dominant wear mechanism in a set of grinding tools operating under various grinding conditions. In this paper it is shown that the addition of nitrogen to methane and hydrogen process gases may be used to influence the surface morphology and structure of the films such that they become suitable for use on micro-tools. The effects of substrate biasing and abrasion on the nucleation and growth of N-doped diamond films, and their influence on the wear of micro-tools is discussed.

10.2. Analysis of Stress in a Loaded Wedge

Diamond grains are angular in habit and possess sharp cutting points prior to grinding workpiece materials. When deposited on a tool substrate, these grains can be considered to be representative infinite wedges. An infinite wedge represents the cutting point of a diamond grain in contact with the workpiece material (Figure 10.1).

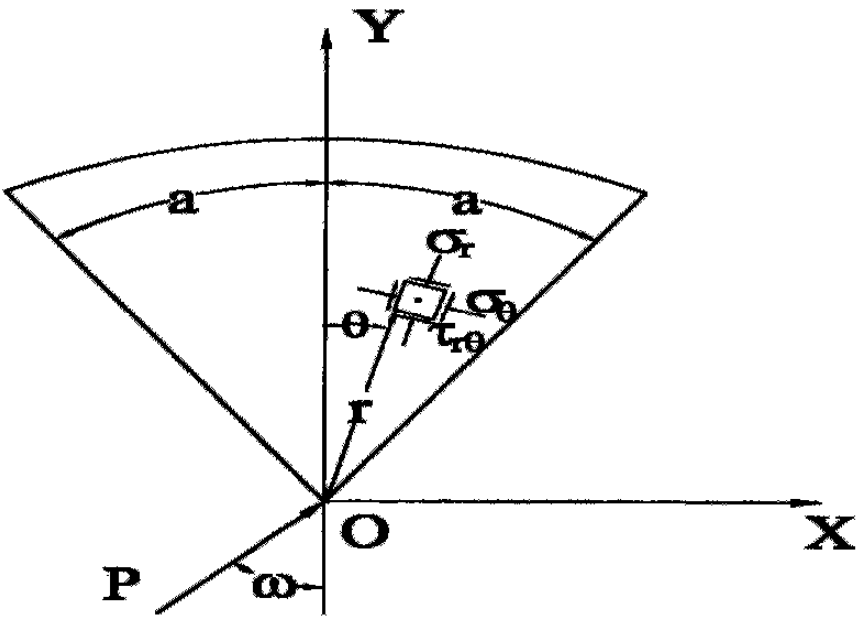

Figure 10.1. The single-point, loaded infinite wedge

The wedge is loaded at the apex by a load P in an arbitrary direction at angle ω to the axis of symmetry of the wedge. Resolving the force into components P.cosω in the direction of the axis, and P.sinω perpendicular to that the stresses due to each of these forces can be evaluated from two-dimensional elastic theory [23]. The state of stress in the wedge, due to force P.cos ω, can be obtained from the stress function,

$$\phi = C.r.\theta.\sin\theta \tag{10.2}$$

Where r and θ are polar coordinates at the point N in Figure 10.2, and C is a constant. The stress function yields the following radial, tangential, and shear stress components,

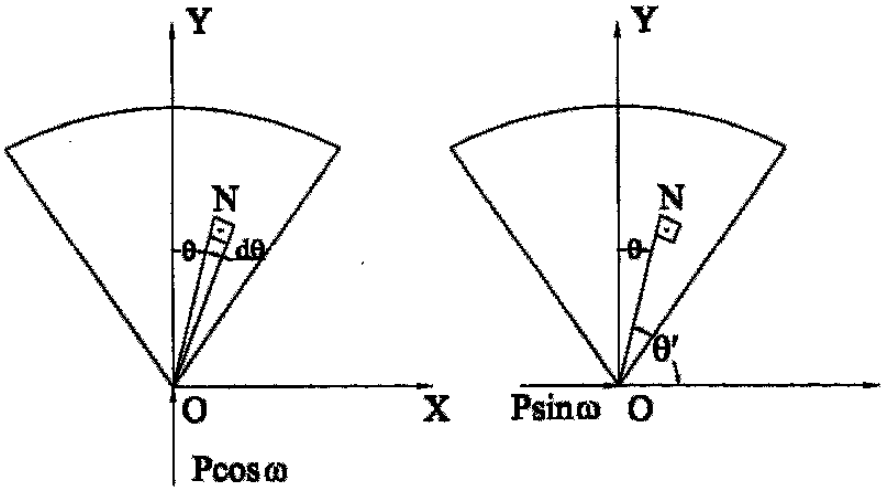

Figure 10.2. The single-point, loaded infinite wedge showing force components, and the point N within the wedge at polar co-ordinates, r and θ

$$\sigma_r = -2C\frac{\cos\theta}{r} \tag{10.3}$$

$$\sigma_\theta = 0 \tag{10.4}$$

$$\tau_{r\theta} = 0 \tag{10.5}$$

To determine the constant, C, the equilibrium of forces along the Y-axis is,

$$P\cos\omega - \int_{-a}^{a} \sigma_{r.} \cos\theta dA = 0 \tag{10.6}$$

Where dA is an element of cross sectional area within the wedge. If, t, is the thickness of wedge, then,

$$\cos\omega P = \int_{-a}^{a} 2C\frac{\cos\theta}{r}.t.r.\cos\theta d\theta \quad = 2Ct\int_{-a}^{a}\cos^2\theta d\theta \quad = \text{Ct (2a + sin 2a)}$$

(10.7)

Therefore, $$C = \frac{P\cos\omega}{t(2a+\sin 2a)} \tag{10.8}$$

And $$\sigma_r = -\frac{2P\cos\theta.\cos\omega}{r.t(2a+\sin 2a)} \tag{10.9}$$

Note that the negative sign denotes that the stress is compressive in this region. The state of stress in the point-loaded wedge, due to force P.sin ω, can be obtained from the following stress function,

$$\phi = C'.r.\theta'.\sin\theta' \tag{10.10}$$

Therefore,

$$\sigma_r = -2C\frac{\cos\theta'}{r} \tag{10.11}$$

And, $$\sigma_\theta = 0 \tag{10.12}$$

$$\tau_{r\theta} = 0 \tag{10.13}$$

Equilibrium of forces along the X-axis (Figure 10.2) yields the following solution for the constant, C,

$$P\sin\omega - \int_{\pi/2-a}^{\pi/2+a} \sigma_r .t.r.\cos\theta' d\theta' = 0 \tag{10.14}$$

$$P\sin\omega = -\int_{\pi/2-a}^{\pi/2+a} 2C\frac{\cos\theta'}{r}.t.r.\cos\theta' d\theta' \; = 2Ct.\int_{\pi/2-a}^{\pi/2+a} \cos^2\theta' d\theta' \; = \text{- C.t}$$

(2a – sin2a)

(10.15)

$$C = \frac{P\sin\omega}{t(2a-\sin 2a)} \tag{10.16}$$

Thus,

$$\sigma_r = -\frac{2P\cos\theta'.\sin\omega}{r.t(2a-\sin 2a)} \tag{10.17}$$

Expressing in terms of the angle θ (where θ' is negative), yields,

$$\sigma_r = -\frac{2P\cos\theta.\sin\omega}{r.t(2a-\sin 2a)} \tag{10.18}$$

Therefore, the combined stresses are,

$$\sigma_r = -\frac{2P}{r.t}\left[\frac{\cos\omega\cos\theta}{2a+\sin 2a} + \frac{\sin\omega\cos\theta}{2a-\sin 2a}\right] \tag{10.19}$$

It follows that the radial stress, σ_r, vanishes for angle θ_o defined using the expression,

$$\tan\theta_o = \frac{1}{\tan\omega}.\frac{2a-\sin 2a}{2a+\sin 2a} \tag{10.20}$$

This equation corresponds to a straight line through the apex as shown in Figure 10.3. This natural axis separates the regions of compressive and tensile stresses in the wedge. It can be seen that for values of angle ω which gives, $|\theta_o| > |a|$, provides a neutral axis that lies outside the included angle of the wedge. This means that the whole area of the wedge will be under stresses of uniform sign. Expressing equation (10.19) in terms of the rake angle of the diamond grain, β, and force components F_t and nF_t (Figure 10.3), yields,

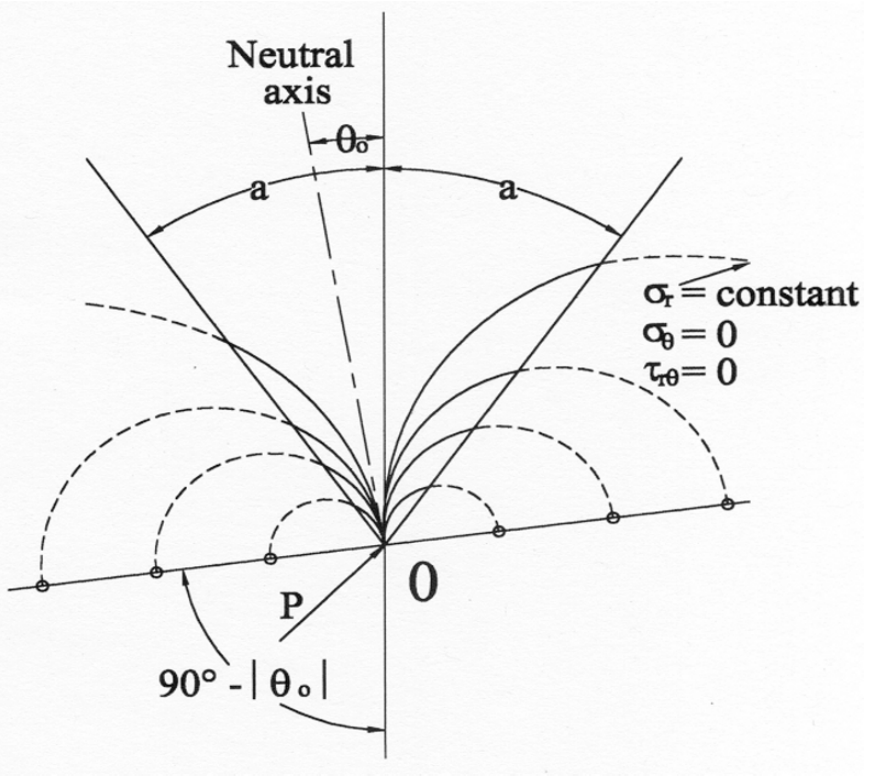

Figure 10.3. Stress analysis of a single-point loaded wedge

$$\sigma_r = -\frac{2F_t}{r.t}\left\{\frac{[n.\cos(a-\beta)+\sin(a-\beta)]\cos\theta}{2a+\sin 2a} + \frac{[\{\cos(a-\beta)-n.\sin(a-\beta)\}\cos\theta]}{2a-\sin 2a}\right\} \quad (10.21)$$

It is observed that,

$$\tan\omega = \frac{\cos(a-\beta)-n.\sin(a-\beta)}{n.\cos(a-\beta)+\sin(a-\beta)} \quad (10.22)$$

In the simple case of a wedge with the normal force nF_t along the wedge axis, a is equal to β, hence,

$$\tan\omega = 1/n \quad (10.23)$$

It is interesting to examine the radial stresses on the left-hand face of the wedge, which corresponds to the leading face of idealised wedge. Thus, for the left-hand face, θ is equal to –a, and from equation (10.19),

$$\sigma_r = -\frac{2P}{r.t}\left[\frac{\cos\omega\cos a}{2a+\sin 2a} + \frac{-\cos a.\sin\omega}{2a-\sin 2a}\right] \quad (10.24)$$

This stress is zero, i.e., the neutral axis coincides with the left-hand limit of the wedge, when,

$$\frac{1}{\tan\omega} = \frac{\sin a(2a+\sin 2a)}{\cos a(2a-\sin 2a)} \quad (10.25)$$

Thus if,

(a) a = β, then,

$$n = \frac{\sin a}{\cos a} . \frac{2a + \sin 2a}{2a - \sin 2a} \tag{10.26}$$

(b) $a - \beta = \frac{\pi}{2} - a$ (as is the case when F_t is parallel to the right-hand face of the wedge).

From equation (10.23),

$$\tan \omega = \frac{\sin a - n.\cos a}{n.\sin a + \cos a} = \frac{\sin a - n\cos a}{n.\sin a + \cos a} \tag{10.27}$$

And substituting in (10.25), yields,

$$\frac{n\sin a + \cos a}{\sin a - n\cos a} = \frac{\sin a}{\cos a} . \frac{2a + \sin 2a}{2a - \sin 2a} \tag{10.28}$$

Therefore,
$$\frac{\frac{1}{2}.n\sin 2a + \cos^2 a}{\sin^2 a - \frac{1}{2}.n.\sin 2a} = \frac{2a + \sin 2a}{2a - \sin 2a} \tag{10.29}$$

$$\frac{1}{2}.n.\sin 2a(2a - \sin 2a) + 2a\cos^2 a - \cos^2 a.\sin 2a =$$

$$= 2a.\sin^2 a + \sin^2 a.\sin 2a - \frac{1}{2}.n.\sin 2a(2a + \sin 2a)$$

$$\frac{1}{2}.n.\sin 2a(2a - \sin 2a + 2a\sin 2a) = 2a(\sin^2 a - \cos^2 a) + \sin 2a$$

$$n.2a.\sin 2a = -\ 2a.\cos 2a + \sin 2a$$

Hence,

$$n = \frac{1}{2a} - \cot 2a \tag{10.30}$$

Equation (0.25) expresses the condition for the whole of the wedge's cross sectional area to be under the influence of a compressive stress. It can be seen that this depends not only upon the rake angle, β, but also upon the force ratio, n. In general the relative size of the region of compressive stresses to the region of tensile stresses depends upon β and n, as equation (10.20) and (10.22) indicate. Also, from equation (10.21), the magnitude of the stress on the left-hand face of the wedge is found to be dependent upon the tangential force component, F_t, and the force component ratio, n. Referring to equation (10.19), it can be seen that for constant stress, σ_r = constant,

$$r.\ C_1 = C_2.\cos\theta + C_3.\sin\theta \tag{10.31}$$

Where C_1, C_2, C_3 are constants. Equation (10.31) represents, in polar co-ordinates, the circumference of a circle tangent to the line. Therefore,

$$C_2.\cos\theta + C_3.\sin\theta = 0 \tag{10.32}$$

i.e., to the neutral axis at the point when r = 0. However, the point r = 0 must be considered separately because the stress at that point approaches infinity, since by definition P is a point load. The central point of these circles are of constant radial stress, and so the point of constant maximum shear stress must lie on a line perpendicular to the neutral axis at the point where r is equal to zero. The radius of each of those circles depends upon the magnitude of the radial stress, σ_r. Maximum values of stress were computed for a variety of point loads and then correlated to the relevant wear parameter, grinding ratio, for a variety of micro-tools. However, this may not represent the real situation where loads may be distributed along the rake face. Further analysis is required that consider point loads distributed along the rake face.

10.3 Stress Analysis in a Wedge with a Distributed Load

Consider an infinite wedge of included angle, 2a, loaded on one face with a linearly distributed normal and shear load as demonstrated in Figure 10.4. Within the loaded region of the wedge, the two-dimensional stress components in the wedge can be found using the plane stress function quoted by Timoshenko and Goodier [23] for wedges under polynomial distributed load. In polar co-ordinates, the stress function is,

$$\phi = a_0 \log r + b.r^2.\log r + c_0 r^2.\log r + d_0.r^2\theta + a_0'\theta + \frac{a_1}{2} r\theta \sin\theta$$

$$+ (b_1.r^3 + a_1'r^{-1} + b_1'r\log r)\cos\theta - \frac{c_1}{2} r\theta\cos\theta$$

$$+ (d_1 r^3 + c_1'r^{-1} + d_1'r\log r)\sin\theta + \sum_{n=2}^{\infty}(a_n r^n + b_n.r^{n+2} + a'r^{-n} + b_n'r^{-n+2}\cos n\theta$$

$$+ \sum_{n=2}^{\infty}(c_n r^n + d_n r^{n+2} + c_{n'}.r^{-n} + d_n'r^{-n+2})\sin n\theta$$

(10.33)

The stress components in the radial, circumferential, and shear directions are,

$$\sigma_r = \frac{1}{r}\frac{\partial\phi}{\partial r} + \frac{1}{r^2}\frac{\partial^2\phi}{\partial\theta^2}, \qquad \sigma_\theta = \frac{\partial^2\phi}{\partial r^2},$$

$$\tau_{r\theta} = \frac{1}{r^2}\frac{\partial\phi}{\partial\theta} - \frac{1}{r}\frac{\partial^2\phi}{\partial r\partial\theta}$$

Considering the terms containing, r^n, and assuming that $n \geq 0$, the radial stress in the wedge is,

$$\sigma_r = 2b_0 + 2d_0 - 2a_2 \cos 2\theta - 2c_2 \sin 2\theta$$
$$+ r(2b_1 \cos\theta + 2d_1 \sin\theta - 6a_3 \cos 3\theta - 6c_3 \sin 3\theta$$
$$- 12r^2(a_4 \cos 4\theta + c_4 \sin 4\theta) - r^n\{(n^2 - n - 2)(b_n \cos n\theta + d_n \sin n\theta$$
$$+ (n+1)(n+2)[a_{n+2} \cos(n+2)\theta + c_{n2} \sin(n+2)\theta]\}$$

(10.34)

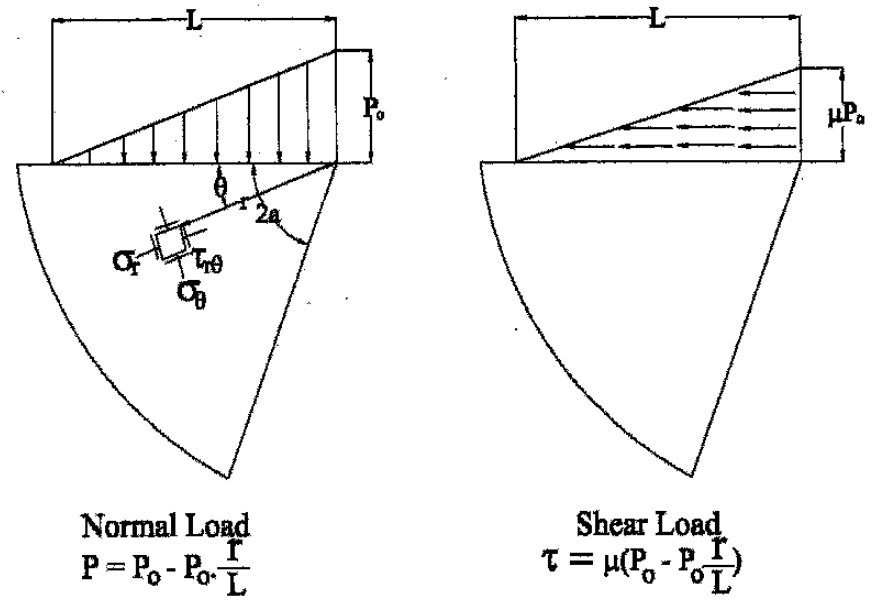

Figure 10.4. Single-point infinite wedge with a linearly distributed normal and shear load

Similarly, the circumferential stress in the wedge is,

$$\sigma_\theta = 2b_0 + 2d_0\theta + 2a_2 \cos 2\theta + 2c_2 \sin 2\theta$$
$$+ 6r(b_1 \cos\theta + d_1 \sin\theta + a_3 \cos 3\theta + c_3 \sin 3\theta)$$

$$+12r^2(b_2\cos 2\theta + d_2\sin 2\theta + a_4\cos 4\theta + c_4\sin 4\theta$$
$$+(n+1)(n+2)r^n[b_n\cos n\theta + d_n\sin n\theta$$
$$+a_{n+2}\cos(n+2)\theta + c_{n+2}\sin(n+2)\theta \tag{10.35}$$

And, the shear stress component in the wedge is,

$$\tau_{r\theta} = -d_0 + 2a_2\sin 2\theta - 2c_2\cos 2\theta$$
$$+r(2b_1\sin\theta - 2d_1\cos\theta + 6a_3\sin 3\theta - 6c_3\cos 3\theta)$$
$$+r^2(6b_2\sin 2\theta - 6d_2\cos 2\theta + 12a_4\sin 4\theta - 12d_4\cos 4\theta)$$
$$+r^n[n(n+1)b_n\sin n\theta - n(n+1)d_n\cos n\theta$$
$$+(n+1)(n+2)a_{n+2}\sin(n+2)\theta - (n+1)(n+2)d_{n+2}\cos(n+2)\theta] \tag{10.36}$$

The boundary conditions to be satisfied in the model are,

$$\sigma_\theta]_{\theta=0} = -(P_0 - P_0\frac{r}{L}), \sigma_\theta]_{\theta=2a} = 0 \tag{10.37}$$

$$\tau_{r\theta}]_{\theta=0} = -\mu(P_0 - P_0.\frac{r}{L}), \tau_{r\theta}]_{\theta=2a} = 0 \tag{10.38}$$

Applying the boundary conditions to equations (10.35) and (10.36) yields the following two sets of simultaneous equations,

$$\left.\begin{aligned} &2b_0 + 2a_2 = -P_0 \\ &2b_0 + 2d_0.2a + 2a_2\cos 2(2a) + 2c_2\sin 2(2a) = 0 \\ &-d_0 - 2c_2 = -\mu P_0 \\ &-d_0 + 2a_2\sin 2(2a) - 2c_2\cos 2(2a) = 0 \end{aligned}\right\}$$

And,

$$\left.\begin{aligned} &6(b_1 + a_3) = \frac{P_0}{L} \\ &b_1 \cos(2a) + d_1 .\sin(2a) + a_3 \cos 3(2a) + c_3 \sin 3(2a) = 0 \\ &-2d_1 - 6c_3 = \mu \frac{P_0}{L} \\ &2b_1 \sin(2a) - 2d_1 \cos(2a) + 6a_3 \sin 3(2a) - 6c_3 \cos 3(2a) = 0 \end{aligned}\right\}$$

The simultaneous equations yield the following values for the unknowns,

$$a_2 = \frac{P_0}{4}\left[\frac{(\mu(2a)-1)\tan^2(2a) + \mu(\tan(2a) - 2a)}{(\tan(2a) - 2a)\tan(2a)}\right]$$

$$b_0 = -\frac{P_0}{2}\left\{1 + \frac{1}{2}\left[\frac{(\mu(2a)-1)\tan^2(2a) + \mu(\tan(2a) - 2a)}{(\tan 2a) - 2a)\tan(2a)}\right]\right\}$$

$$c_2 = \frac{P_0}{4}\left[\frac{1 - 2\mu(2a) + \mu\tan(2a)}{\tan(2a) - 2a}\right]$$

$$d_0 = \frac{P_0}{2}\left[\frac{\mu\tan(2a) - 1}{\tan(2a) - 2a}\right]$$

$$a_3 = \frac{P_0}{24L}\left[\frac{\tan^2(2a) + 3 - 6\mu\tan(2a)}{\tan^2(2a)}\right]$$

$$c_3 = -\frac{P_0}{24L}\left[\frac{3\mu\tan(2a)(\tan^2(2a)-1)+2}{\tan^3(2a)}\right]$$

$$b_1 = \frac{P_0}{8L}\left[\frac{\tan^2(2a)-1+2\mu\tan(2a)}{\tan^2(2a)}\right]$$

$$d_1 = \frac{P_0}{8L}\left[\frac{2-\mu(\tan^2(2a)+3)\tan(2a)}{\tan^3 2a}\right]$$

The stresses can now be computed anywhere in the loaded region of the wedge. For the point, r = 0, the angle, θ, is equal to zero, i.e., at the apex of the wedge an arbitrary choice of shear loading on the two faces of the wedge will not produce equilibrium conditions. This is observed if the edge is taken as a 90° corner, and shear loading is considered on one face only. The clearance face is free from shear stress and the corner element is not in equilibrium. Assuming that the error is small, the radial stress, σ_r, at the apex (from equation (10.34) and for r = 0, then θ = 0), is,

$$\sigma_r]_{\substack{r=0\\ \theta=0}} = 2(b_0 - a_2)$$
$$= -P_0\left[\frac{2a\tan(2a)(\mu\tan 2a)-1)+\mu(\tan(2a)-2a)}{(\tan(2a)-2a)\tan(2a)}\right]$$

(10.39)

The analysis shown can be applied to any type of polynomial distribution of the load over the rake face of the wedge-shaped abrasive grain. If the force distribution is not polynomial, an approximate solution can be obtained by considering a linearly

distributed load that is equivalent to the original one. Maximum values of stress were computed for a variety of distributed loads and then correlated to the relevant wheel wear parameter, grinding ratio, for a variety of micro-tools.

10.3.1 Development of Wear Model

Brittle materials exhibit high strength properties when loaded in compression than in tension. The ratio of rupture strengths is usually between 3:1 and 10:1 [24]. The existence of relatively low tensile stresses in the diamond grains, may cause failure by fracture to occur. To alleviate fracture, it is possible to use larger grains that reduce the stress levels in the grain when subjected to grinding forces. The effects of changing the amount of nitrogen in the gaseous mixture when creating diamond grains has the effect of changing morphology and the sizes of grains. Therefore, special attention must be paid to deposition conditions that will optimise the size and shape of diamond grains that will resist negative tensile stresses established in the grains when grinding takes place. Therefore, processing conditions determine the life of diamond grains when subjected to large grinding forces. To measure the effectiveness of the deposition process, it is required to model the effects of tensile stresses on the fracture properties of diamond grains deposited in various gaseous environments in order to quantify the effects of nitrogen on the life of micro-tools.

To model the action of the micro-tool, we must consider a single active cutting point to be classed as a wedge of constant width loaded at its inverted apex with point loads, F, and, nF, which represent the radial and tangential force components with reference to the micro-tool in which the grain is supported, and P is the resultant force (Figure 10.5). The stress distributions within point-loaded wedges can be determined analytically, and the results of such an analysis indicate that if tensile stresses exist within the wedge then it will occur at its maximum along the rake face. The existence of a tensile stress depends on the magnitude of the force ratio, n. If the ratio is especially small that a tensile stress exists in the wedge, then for a specific force ratio the tensile stress is

proportional to the tangential grinding force, F. Stresses of this nature would extend to and beyond the diamond grain-substrate interface. The fracture of diamond grain and the interface between the substrate depends on the particular micro-tool used and the magnitude of the tensile stress induced during grinding. Grains of diamond are typically seven-to-ten times stronger in compression than in tension, and therefore the probability of grain fracture is likely to increase with an increase in tensile stress exerted in the grain although the magnitude of the stress may be slightly higher than one-fifth the magnitude of the maximum compressive stress in the grain. A significant barrier to the acceptance of stress patterns evaluated for such situations arises because point loads applied to perfectly sharp wedges produce infinitely high stresses at, and about, the point of contact. Therefore, the loads must be applied over a finite area. This implies that compressive stresses dominate over the finite area. Experimental results [24] show that rake face stresses are compressive over the entire length of chip-tool contact but are tensile outside of this region. The zone of fracture initiation points were located in the tensile zone at about two to two-and-a-half times the chip-tool contact length.

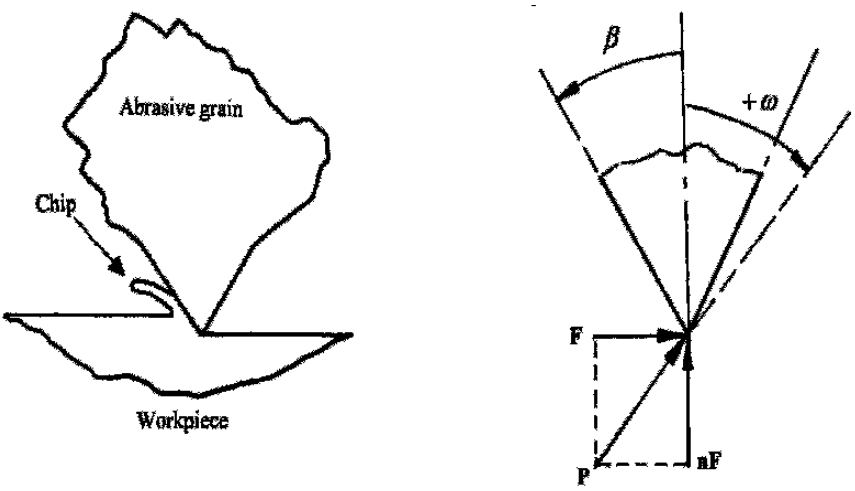

Figure 10.5. Ideal wedge-shaped cutting point and grinding force diagram

It seems likely that higher tensile stresses are associated with higher grain fracture probability resulting in rapid loss of diamond grains and, consequently, lower grinding ratios. The wear model should incorporate the fact that the loads are spread over a finite area. This implies that single-point loads are resolved into multiple point loads along the rake face, or are indeed, applied directly along the rake face of the cutting tool. The model should allow the relationship between the wear of a micro-tool and the general nature of stresses established in active diamond grains subjected to grinding forces to be examined. However, the development of a wear model that represents the effects of induced stress in the material is required. The analytical models developed here describe well the initial stages of grinding. However, as the grains are worn by a mechanism of abrasive wear rather than fracture wear, then a computational model must be considered.

10.3.2 Computational Stress Analysis of Single Diamond Grains

The assumed geometry of an ideal grain in the vicinity of its cutting edge is a simple symmetrical wedge of constant width with an included angle of 70^{O} that results in a rake angle of -35^{O}. There is no wear flat on the model cutting grain. In order that a finite element method is used to evaluate stresses in the wedge, the wedge was subdivided into 210 diamond-shaped elements with a total of 251 nodes. Forty-one nodes were constrained at the boundary of the wedge and the leading five nodes on the rake face were loaded (Figure 10.6). The tangential and normal grinding point loads were replaced by a series of multiple loads (F_Y and F_Z) acting perpendicular to (normal load) and along (shear load) the rake face of the wedge.

The loads at the five nodes are representative of the distributed and normal loads acting on the rake face over the diamond grain-chip contact length. The normal force distribution on the rake face was taken as being a maximum value at the cutting edge and decreases linearly to zero at the end of the diamond grain-chip contact length. The shear force was taken to be constant over the

first half of the contact length, decreasing linearly to zero over the contact length. Grinding loads were also applied directly to the rake face and at the tip of the diamond without applying multiple loads along the rake face. This was performed in order to compare and contrast the effect of different force distributions on the stresses generated within the diamond wedge.

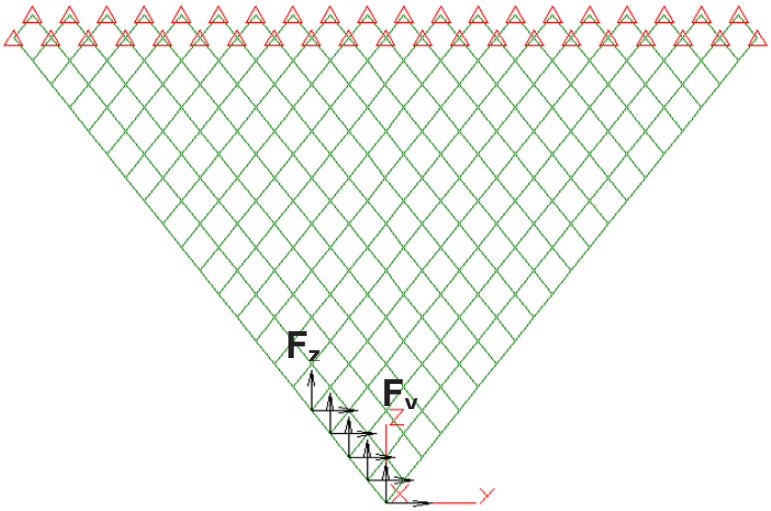

Figure 10.6. Finite element assemblage with grinding loads applied at the rake face nodes

To measure the value of using the maximum tensile stress as a way to estimate grain fracture tendency, the correlation between the two sets of data were calculated for each set of data. The region of fracture initiation was also located using Griffith's criterion of fracture [26], which is applicable to the fracture of brittle materials. For,

$$\frac{\sigma_c}{\sigma_t}.\sigma_1 + \sigma_3 > 0 \qquad (10.33)$$

Then,

$$\sigma_1 = \sigma_t \tag{10.34}$$

But for,

$$\frac{\sigma_c}{\sigma_t}.\sigma_1 + \sigma_3 < 0 \tag{10.35}$$

Then,

$$\left(|\sigma_1| - |\sigma_3|\right)^2 + 8\sigma_t\left(|\sigma_1| - |\sigma_3|\right) = 0 \tag{10.36}$$

Where σ_1 and σ_3 are the principal stresses, assuming that $\sigma_1 > \sigma_3$, σ_t is the ultimate tensile strength of the abrasive grain, and σ_c is the ultimate compressive strength. For diamond, the ratio of σ_t and σ_c is approximately 0.1.

10.4 Experimental Methods

10.4.1 Hot filament chemical vapor deposition

The hot filament CVD system is composed of a water-cooled stainless-steel vessel, which is connected to a rotary pump enabling a vacuum to be produced. The hot filament CVD apparatus is shown in Figure 10.7. Gas flow rates are controlled using MKS mass flow controllers to accurately control the amounts of gases flowing into the reactor. The system allows independent bias to be applied between the substrate and filament. The filament consisted of a coiled tantalum wire of diameter 0.5 mm to activate the reaction mixture. The filament temperature was measured using an optical pyrometer with values between 2200 and 2500K. Substrate temperatures were measured using a K-type thermocouple in direct thermal contact with the substrate. After abrasion, the samples were

ultrasonically cleaned with acetone prior to deposition. The diamond films were grown on pre-abraded WC-Co substrates for 4 h under standard deposition conditions [4]. To investigate the effects of changing the gas-phase environment different concentrations of nitrogen, from 50 to 100,000 ppm, were added to the standard 1% methane in hydrogen gas mixture. This is equivalent to varying the N/C ratio from 0.01 to 20. The film morphology, growth rate, and quality were characterised using Raman spectroscopy (Kaiser Holo Probe: 532 nm, Nd : YAG laser), and scanning electron microscopy (SEM).

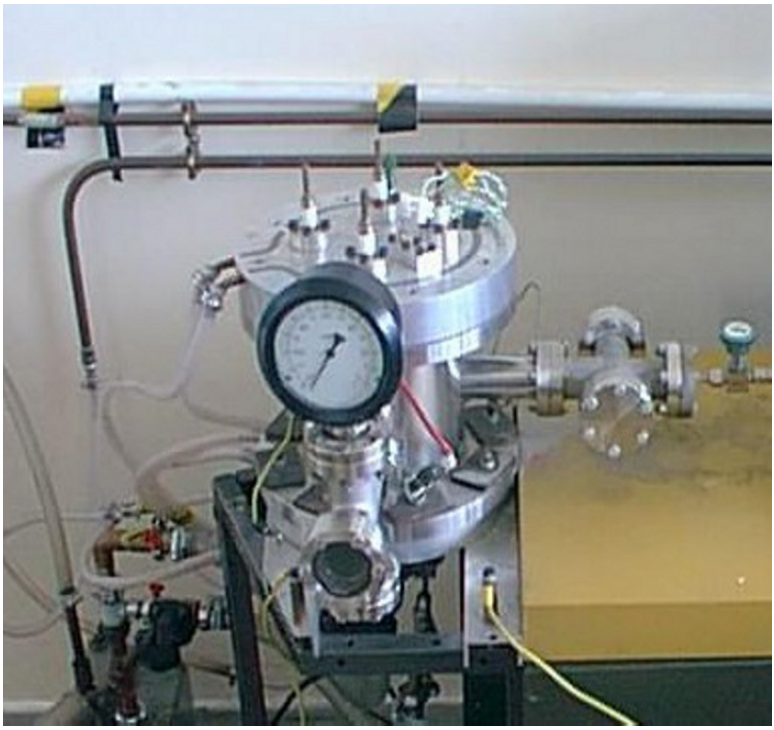

Figure 10.7. Hot filament CVD apparatus

10.4.2 Measurement of wear of diamond tools

The measurement of the wear of diamonds on a single layer deposited to the grinding tool requires grinding various workpiece materials on a specially constructed machine tool. The machine tool

was constructed using a tetrahedral space frame design that attenuates vibrations generated during grinding. The grinding tool is held in an air turbine spindle capable of rotating the grinding tool in excess of speeds of 350,000 revolutions per minute. Figure 10.8 shows the machine tool complete with three axes of motion in the x, y, and z-directions. A fourth axis capable of rotary motion can also be used on the machine tool. The machine tool was used to measure the performance of the grinding tools machining materials such as medium carbon steels (hypoeutectoid), high carbon tool steels (hypereutectoid), and cast iron. Grinding experiments were conducted using a number of micro-tools coated with diamonds that were produced in a hot filament CVD reactor containing gases with varying amounts of nitrogen in a methane/hydrogen mixture. The grinding ratio was measured in accordance with that stated in section 1. However, in order to correlate the magnitude of tensile stress in the diamond grains to the grinding ratio, it is required to know the number of active cutting grains on the surface of the micro-tool.

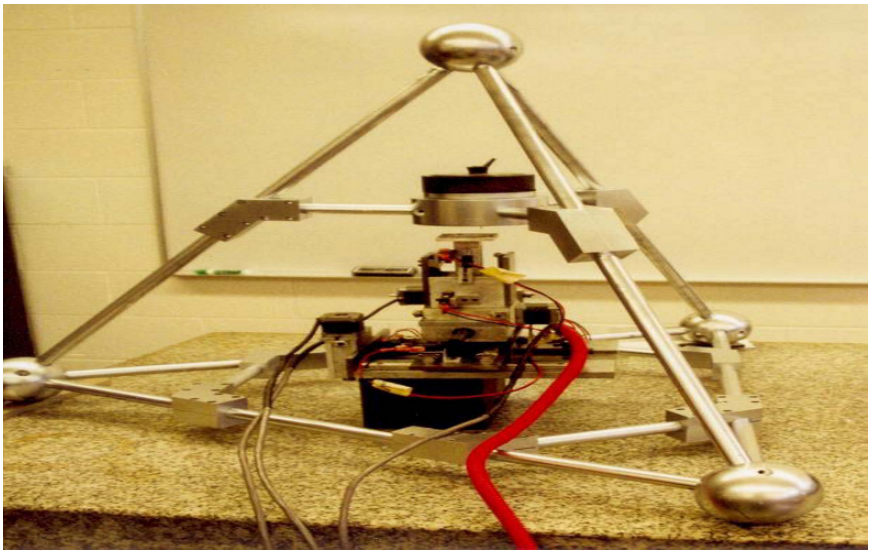

Figure 10.8. Micro-machine tool showing tetrahedral spaceframe surrounding the precision x-y-z table and the extremely high-speed air-turbine spindle

The number of active cutting grains on the micro-tool surface is found quite simply by driving a grinding tool into a piece of soft metal that has a length equal to the grinding tool's circumferential length. The depth to which the grinding tool is driven into the length of soft metal is equal to the depth of cut. The impression that the grinding tool produces in the length of soft metal is equal to the number of cutting points that are active during the grinding stroke at that particular rate of cut. However, the micro-tool must be prepared by simulating the grinding conditions used during the experimental conditions. Once the micro-tool has stabilized at its optimum grinding condition, then the tool is removed from the machine tool and driven into the soft metal that simulates one grinding revolution into the workpiece material. The force components are then applied to a 'model' diamond grain by dividing the grinding force data generated using a dynamometer into the number of active cutting grains over an area that simulates the diamond grain-workpiece contact area over one revolution. Stresses established in this area are calculated using finite elements. The wear of the micro-tool, expressed in terms of a grinding ratio, and its relationship to the stresses set up in the model grain is compared.

10.5 Discussion

10.5.1 Diamond deposition

Figure 10.9 shows CVD diamond growth on unabraded WC-Co substrate for six hours: A striking increase in diamond nucleation density is observed with the presence of nitrogen in the process gas. It is evident that nitrogen enhances the nucleation of diamond. However, even after 6 hours it not sufficient on its own to cause the growth of a continuous diamond film. Hence, surface abrasion or another form of substrate preparation is a necessary in the creation of nucleation sites for the growth of diamond films. Figure 10.10 shows CVD diamond growth with and without surface abrasion. It is clearly evident that without abrasion even after 4 hours of deposition only isolated crystals of diamond appear on the surface of the substrate. However, surface abrasion results in a continuous film of

diamond with the nucleation density of about 9 x 10^8 /cm^2. Mixed crystals of <111> and <100> orientation are formed, which are typically 1-3 μm in diameter. The film is continuous with no evidence of pin-holes, or cracks. For micro-tools, a highly controlled method of surface treatment is desirable. Even though surface abrasion is very effective in creating nucleation sites it does not allow a high degree of precision and control of surface preparation and therefore bias enhanced nucleation has been investigated as an alternative.

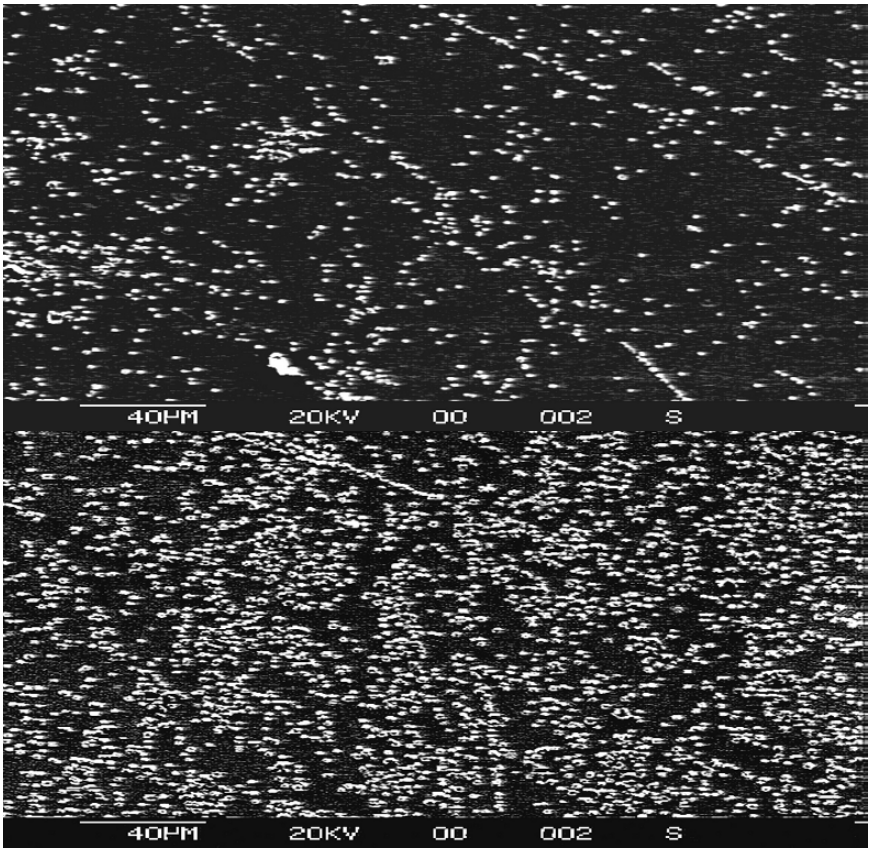

Figure 10.9. Diamond nucleation on the unabraded surface prior to deposition for 6 hour at 0 and 200ppm nitrogen addition

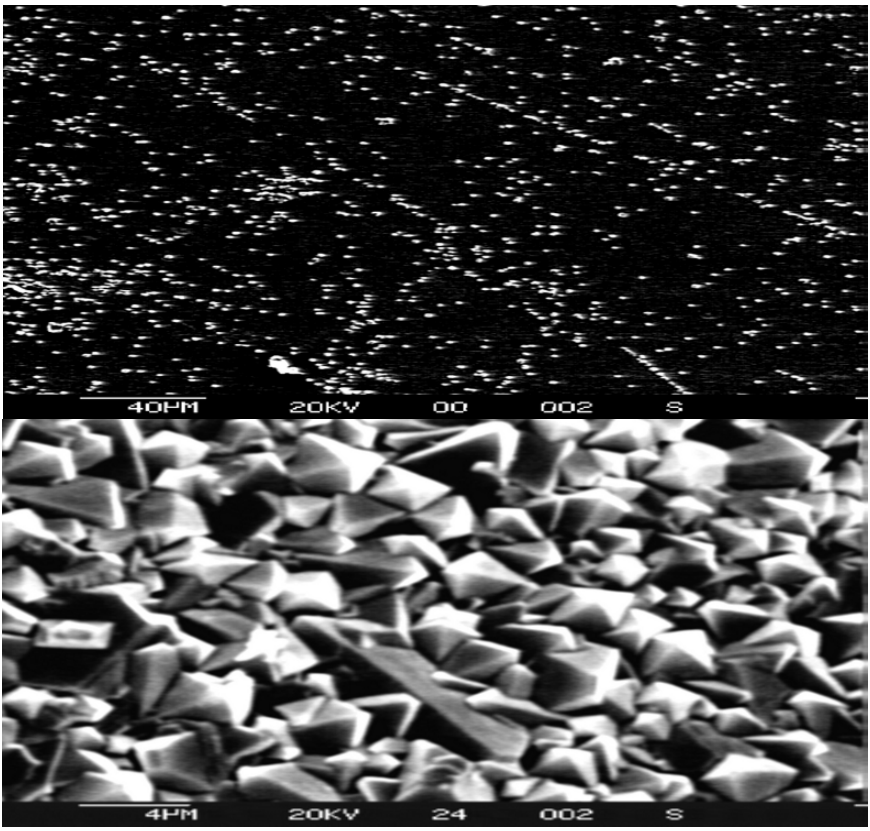

Figure 10.10. Diamond growth: (a) without surface abrasion; and (b) with surface abrasion with a diamond powder

Application of a negative bias of –300V to the substrate for 30 minutes prior to the deposition stage gives a measurable increase in the nucleation density with a continuous film forming (Figure 10.11). The increase in nucleation is due to the creation of nucleation sites arising from ion bombardment of the substrate. However, at the pressures utilised in this study of 2660 Pa the mean free path is relatively small and ion acceleration appears unlikely and an alternative explanation may be more likely. Biasing the substrate changes the composition of the plasma creating a higher concentration of hydrogen radicals near to the substrate and therefore the changes in the morphology could be due to a chemical etching effect rather than an ion bombardment effect. It is evident

from Figure 10.12 that as the amount of nitrogen is increased from 0 to 200ppm the size of diamond crystals also increases. The addition of nitrogen is thus enhancing the growth of the diamond crystals. However, the precise reasons for this growth enhancement are still unclear and are being investigated. Figure 10.13 illustrates that further additions of nitrogen degrade the crystal structure considerably but improves the surface roughness of the films.

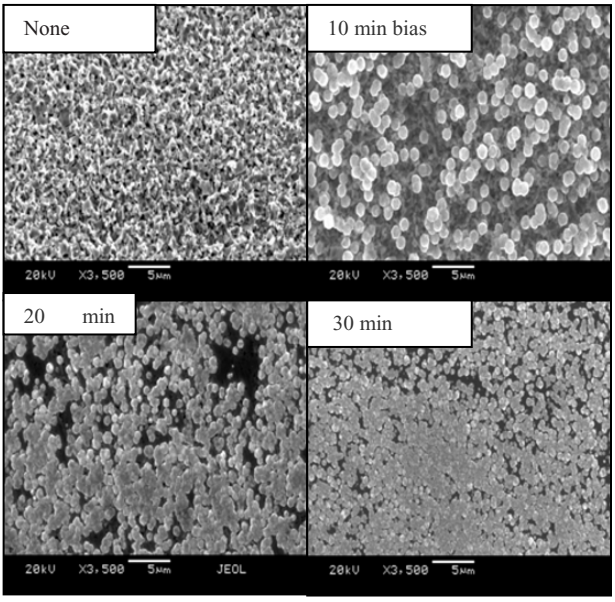

Figure 10.11. Scanning electron micrograph showing the effects of biasing time on the nucleation density

These films were grown under the same conditions but in separate studies. The different grain densities indicate the difficulty in obtaining absolute reproducibility, though the relative density measurements are significant. Raman analysis confirms this trend. For relatively small amounts of nitrogen in the gas phase the FWHM of the 1332 cm^{-1} absorption characteristic of diamond is reduced indicating an increase in the diamond phase purity. For higher levels of nitrogen the diamond peak broadens and disappears altogether with N_2 levels above 50,000 ppm in the gas mixture (Figure 10.14). This data is consistent with films produced from microwave

diamond CVD studies [8]. The changes in the surface morphology and structure are related to the carbon supersaturation, which is controlled by the supply of carbon and the creation of growth sites at the surface [8]. Small amounts of nitrogen are able to reduce carbon supersaturation, which leads to an improvement in crystal quality. At higher levels of nitrogen the carbon supersaturation increases and the morphology changes from blocky to spherical, which is accompanied by deterioration of the diamond phase purity.

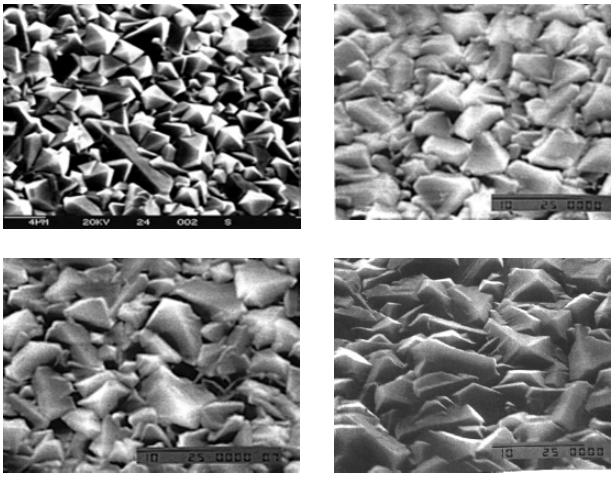

Figure 10.12. N-doped CVD diamond growth at 0, 50, 100 and 200 ppm of nitrogen

10.5.2 Wear of diamonds

The wear of micro-tools coated with diamonds deposited from various gaseous environments doped with nitrogen appears in Table 10.1. Here, it is shown that the nature of the diamond is optimised at 200 parts-per-million of nitrogen in methane/hydrogen mixture. Beyond this value, the grinding ratio decreases because the diamonds are becoming smaller in size and the surface is becoming smoother.

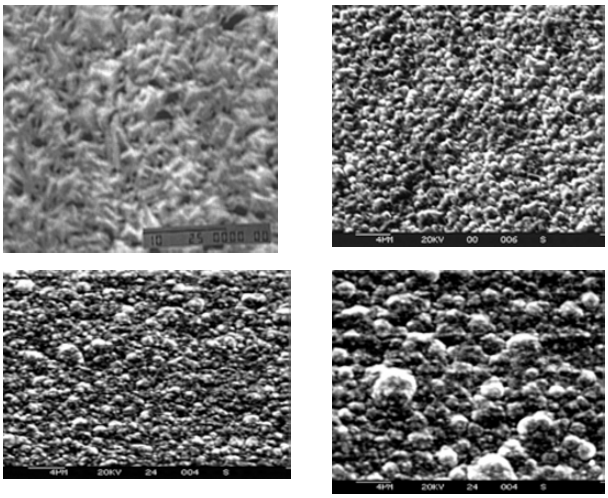

Figure 10.13. N-doped diamond at 5000, 10000, 50000 and 100000 ppm of nitrogen

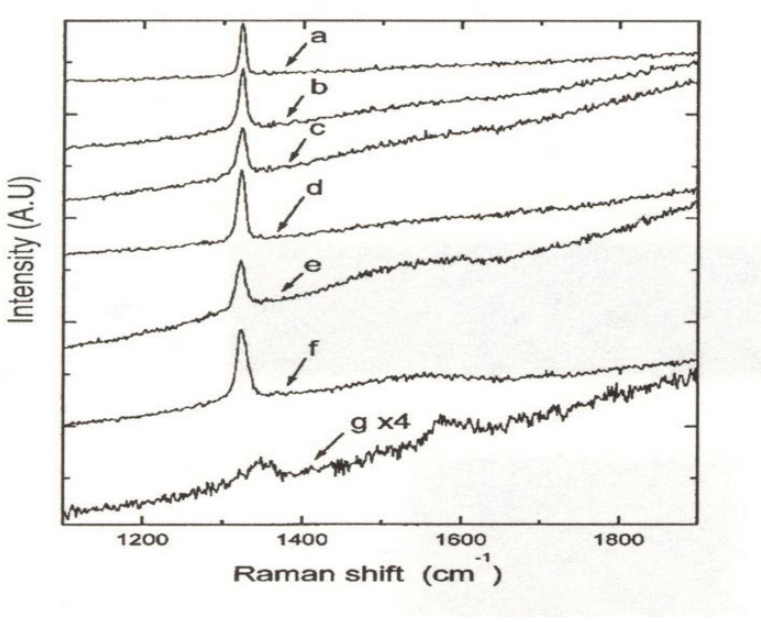

Figure 10.14. Raman spectra of n-doped diamond coatings: (a) 200 ppm; (b) 100 ppm; (c) 5000 ppm; (d) 50 ppm; (e) 10000 ppm; (f) 50000 ppm; and (g) 0 ppm

Below 200 ppm, the diamonds are scattered in random formation producing a discontinuous film of diamonds leaving large areas of the tool unable to grind the surface of the workpiece material. The results of the two-dimensional stress analyses were consistent with the experimentally determined stress distribution obtained by Loladze [25] when cutting soft metal with photoelastic tools. The maximum tensile stress always occurs at the rake face at a distance from the cutting edge ranging from 1.5 – 4 times the abrasive grain-chip contact length, the exact magnitude of the coefficient depends on the loading conditions for a particular grinding event. For a given value of the tangential force component, F, the higher the force ratio, F/nF, the greater the distance the maximum tensile stress is away from the cutting edge. These results indicate that mechanically induced fracture occurs at a finite distance away from the cutting edge. When using Griffith's criterion, the influence of mechanically induced stresses indicate that fracture initiation zones are established. Figure 10.15 shows the occurrence of such zones in an idealized wedge. The first zone is located around the point of maximum tensile stress and is always at the rake face.

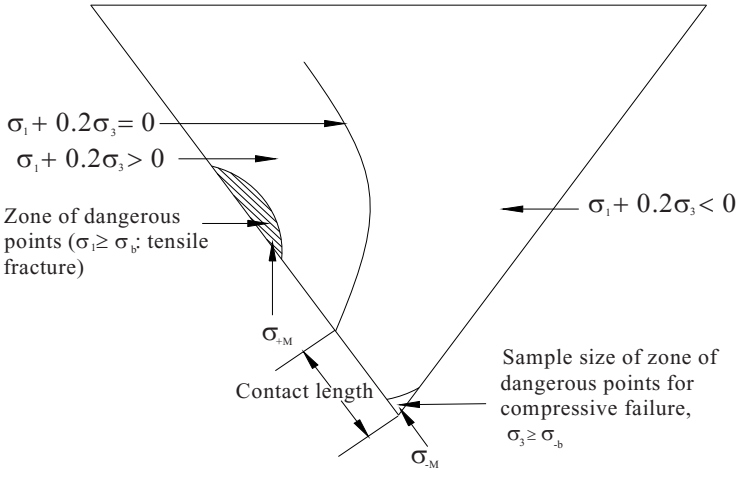

Figure 10.15. Griffith's criterion applied to the idealized wedge showing tensile and compressive fracture initiation zones

Failure in this zone is tensile and would initiate fracture at a point on the rake face of the order of two-to-three times the diamond grain-chip contact length away from the cutting edge. This type of fracture is consistent with fracture on a scale comparable with the chip thickness and tends to produce the so-called 'self-sharpening action'. The second much smaller zone is located at the immediate vicinity of the cutting edge. Failure is compressive in this region and results in 'crumbling' of the cutting edge leading to the formation of a wear flat on the diamond grain.

Nitrogen (ppm in methane/hydrogen mixture)	**Grinding ratio**
0	50
50	110
100	200
200	300
5000	175
10000	85
50000	60
100000	20

Table 10.1. Performance data for grinding normalized M2 tool steel. Grinding conditions: tool diameter: 750μm; spindle speed: 350,000rpm; depth of cut: 10μm; feed rate: 10μm/min

The correlation between the magnitude of the maximum tensile stress in the model diamond grains and the grinding ratio (Table 10.2) is high and is dependent on the way the forces are applied to the grains. It would be expected that the higher the tensile stress, the greater is the rate of grinding wheel wear and consequently the corresponding grinding ratio. Perfect linear correlation in accordance with this would result in a correlation coefficient of –1. The correlation coefficient between the maximum tensile stress and the grinding ratio is significant. This is to be expected as the force ratio may vary slightly. However, if the tangential component of the grinding force changes significantly without a change in force ratio, then it is expected that the maximum tensile stress will change significantly and consequently reduce the grinding ratio.

Workpiece material	Grinding Ratio	Exact wedge model with point loads applied to apex of the wedge	Approximate finite element model: multiple grinding loads applied to rake face of wedge	Approximate finite element model: grinding forces applied directly to the rake face of the wedge
En2 steel (hypoeutectoid)	500	-0.7	-0.82	-0.99
Normalized M2 tool steel	300	-0.54	-0.68	-0.98
En8 steel (hypoeutectoid)	250	-0.15	-0.25	-0.6
AISI 52100 (hypereutectoid)	350	-0.76	-0.86	-0.98
Annealed M2 tool steel	250	-0.8	-0.9	-0.99
Chilled Grey Cast Iron (Flake Graphite)	650	-0.83	-0.85	-0.91
Spheroidal Graphite Cast Iron	580	-0.9	-0.95	-0.99
Austempered Ductile Iron (Bainitic Structure)	525	-0.92	-0.95	-0.99

Table 10.2. Correlation coefficient between maximum tensile stress and grinding ratio for an idealized wedge that simulates a grinding tool that has an optimum diamond coverage using a controlled gas atmosphere of 200ppm of nitrogen in methane/hydrogen mixture. Comparison is also made between the methods of applying loads to the idealized wedge models

The calculation and application of multiple grinding loads along the rake face produces a lower correlation coefficient compared to directly applied grinding loads. This implies that grinding loads are simply not point loads acting act the tip of the inverted apex and along the abrasive grain-chip contact length of the grinding grain. In

fact, directly applied grinding forces produce better correlation coefficients. This means that for perfectly micro-tools, one must apply the component grinding loads directly to the rake face.

10.6 Conclusions

We have shown that the surface morphology of the diamond films can be controlled by employing surface abrasion, substrate biasing, or nitrogen addition to the gas mixture. The application of a bias voltage during normal diamond growth enables re-nucleation of the diamond film. Thus, the crystal size and surface roughness may be controlled with no reduction in the diamond phase purity. Addition of nitrogen to the gas phase during diamond CVD can also be used to control the surface morphology. For diamond-coated microtools, grain fracture appears to be the dominant cause of diamond loss during a grinding operation. Grain fracture is much more likely to be caused by mechanically induced tensile stresses within diamond grains than by mechanically induced compressive stresses. The best indicator of microtool performance during a grinding operation under different operating conditions is the level of tensile stress established in diamond grains. High tensile stresses are associated with grain fracture and low grinding ratios in perfectly sharp micro-tools. Finite element models of sharp diamond grains can be applied to micro-tools where the dominant wear mechanism is grain fracture.

References

[1] Fan Q H, Periera E, Gracio J., Time modulated CVD diamond processing of diamond, J. Mater. Res., 1998, **13**(10), 2787-2794.
[2] May P, Rego C A, Thomas R M, Ashfold M N R, Rosser K N, Everitt N M., CVD diamond wires and tubes, Diamond Related Mater., 1994, **3**, 810-813.
[3] Kostadinov L, Dobrev D, Okano K, Kurosu T, Iida M., Nuclear and growth of diamond from the vapor phase, Diamond Related Mater., 1992, **1**, 157-160.
[4] Ali N, Ahmed W, Hassan IU, Rego CA., Surface engineering of diamond coated tools, Surf. Eng., 1998, **14**(4), 292.
[5] Beckmann R, Kulisch W, Frenck H J, Kassing R., Influence of gas phase parameters on diamond kinematics of thin diamond films deposited by MWCVD and HFCVD techniques, Diamond Related Mater., 1992, **1**, 164-167.

[6] Ojika SI, Yamoshita S, Ishikura T., Diamond growth on copper substrate, Japanese J. Appl. Phys., 1998, **32**(2), L1681-L1683.
[7] Muller-Serbert W, Worner E, Fuchs F, Wild C, Koidl P., Nitrogen induced increase in growth rate in CVD diamond, Appl. Phys. Lett., 1996**,** **68**(6), 759-760.
[8] Bohr B, Haubner R, Lux B., Influence of nitrogen additions on HFCVD diamond, Appl. Phys. Lett., 1996, **68**(8), 1075-1077.
[9] Yarbrough W A, Messier R., Diamond deposition to silicon, Science, 1988, **247**, 688.
[10] Kanetkar S M, Metera G, Chen X, Pramanick S, Tiwari P, Narayan J, Pfei!er G, Paesler M., Growth of diamond on silicon substrates, J. Elect. Mater., 1991;**20**:4.
[11] Wolter S D, Stoner B R, Glass J T, Ellis P J, Jenkins D S, Southworth P., Textured growth of diamond on silicon via in situ carburisation and bias enhanced nucleation, Appl. Phys. Lett., 1993, **62**, 1215-1217.
[12] Jiang X, Klages C P, Zachia R, Hartureg M, Fuser H J., Epitaxial diamond films on (001) silicon substrates, Appl. Phys. Lett., 1993, **62**, 3438-3440.
[13] Stubhan F, Ferguson M, Fusser H J, Behom R J., Heteroepitaxial nucleation of diamond on Si (001) in HFCVD, Appl. Phys. Lett., 1995, **66**, 1900-1902.
[14] Li X, Hayashi Y, Nishino S., Analysis of oriented diamond nucleation processes on silicon substrates by HFCVD, Japanese J. Phys., 1997, **36**, 5197-5201.
[15] Locher R, Wild C, Herres N, Behr D, Koidl P., Nitrogen stabilized <100> texture in CVD diamond films, Appl. Phys. Lett., 1994, **65,** 34-36.
[16] Jin S, Moustakas T D., Effect of nitrogen on the growth of diamond films, Appl. Phys. Lett., 1994, **65**, 403-405.
[17] Borst T H, Munzinger P C, Weiss O., Characterization of undoped and doped homoepitaxial diamond layers produced by microwave plasma CVD, Diamond Related Mater., 1994, **3**, 515-519.
[18] Koizumi S, Kamo M, Sato Y, Mita S, Sauabe A, Reznik C, Growth and characterization of phosphorous doped n-type diamond films, Diamond Related Mater., 1998, **7**, 540-544.
[19] L. P. Tarasov, Grindability of Tool Steels, American Society of Metals, 1951, **43**, 1144 – 1151.
[20] H.K. Tonshoff and T. Grabner, Cylindrical and profile grinding with boron nitride wheels, Proceedings of the 5th International Conference on Production Engineering, Japanese Society of Precision Engineers, p.326, 1984.
[21] S. Malkin and N. H. Cook, The wear of grinding wheels – Part 1: attritious wear, Trans. A.S.M.E. – Journal of Engineering for Industry, 1971, **93**, 1120 – 1128.
[22] M. J. Jackson, Vitrification heat treatment during the manufacture of corundum grinding wheels, Journal of Manufacturing Processes, 2001, **3**, 17-28.
[23] S. P. Timoshenko and J. N. Goodier, Theory of Elasticity, 3rd Edition – International Student Edition, McGraw-Hill Kogakusha Ltd., p.p. 109-113, and p.p. 139-144, 1970.

[24] A. G. King and W. M. Wheildon, Ceramics in Machining Processes, (Academic Press, New York, 1966).
[25] T. N. Loladze, Requirements of tool materials, Proceedings of the 8th International Machine Tool Design and Research Conference, Pergamon Press, 821-842, 1967.
[26] A. A. Griffith, The phenomena of rupture and flow in solids, Philosophical Transactions of the Royal Society of London, 1921, **A221**, 163-198.